Chapter 4

Optical-Fiber-Based Measurement of an Ultrasmall Volume, High-Q Silicon Photonic Crystal Microcavity

4.1 Introduction

This chapter details the measurements of photonic crystal microcavities within silicon membranes. The cavity design is the graded square lattice geometry described in chapter 2 and examined experimentally within InP-based multi-quantum-well membranes in the previous chapter. From a device performance perspective, the primary result of importance in this chapter is the demonstration of a quality factor $Q \sim 40,000$ in a wavelength-scale PC cavity. Of equal importance, however, is the development of an optical-fiber-based probing technique that is utilized to study the spectral and spatial properties of resonant modes within these PC cavities. This technique, which essentially involves evanescent coupling between an optical fiber taper waveguide and the PC cavity, allows for quantitative measurements of two of the most important properties of a cavity mode, its Q and spatial localization (related to V_{eff}). From an experimentalist's perspective, other benefits of this fiber-based probing method are that it is relatively easy to implement and can be used to rapidly characterize all of the devices on a chip.

The majority of this chapter (sections 4.2-4.7) is largely based on three articles; (i) ref. [52], which describes our initial use of the fiber taper to demonstrate a high Q ($\sim 40,000$) and spatial localization consistent with an ultrasmall V_{eff} ($\sim 0.9(\lambda/n)^3$) in a PC cavity, (ii) ref. [53], which uses the fiber-based probe to study the robustness of the cavity Q in our graded lattice design with respect to perturbations in the lattice, and (iii) ref. [54], which is a review article that we have written on the use of the fiber taper as a probe for PC microcavities (and wavelength-scale semiconductor cavities in general).

In section 4.8, I briefly review some of the work that I was not the primary investigator on, but which I had the opportunity to be a part of and is directly related to the work described in this and subsequent chapters. The first topic [57] describes the work of my colleague Paul Barclay in coupling light into our PC microcavities through use of an intermediate PC waveguide that is phase matched to the fiber taper. This technique is critical in achieving coupling to the cavities that is far more efficient than what is achieved through direct coupling from the fiber taper. The second topic I examine is the work of Matt Borselli [64], who used fiber tapers to investigate Si microdisk cavities. Matt was able to demonstrate Q/V ratios that were slightly higher than what we saw in the PC cavities, and more importantly, was able to show that the fiber taper can directly couple light into these devices in a relatively efficient manner. His work on these structures led to my subsequent adoption of them in experiments involving AlGaAs microcavities with embedded quantum dots (chapters 5-7).

4.2 Fabrication

We decided to fabricate our PC cavities within the silicon-on-insulator (SOI) material system, due to its relatively low material loss in the 1.5 μm range and how readily available it is commercially. The material, obtained from the company SOITEC, consists of a 340 nm thick silicon (Si) layer on top of a 2 μm silicon dioxide layer. As our goal was to test our devices through evanescent coupling with fiber tapers, we decided to fabricate our cavities on mesas that are isolated from the rest of the chip (the specific reasons for this, and recent developments that have obviated it, are discussed later within the chapter). The following processing steps were performed (additional details are given in appendix C): (1) electron beam lithography of the PC pattern and accompanying cutouts for removal of additional material from the mesa, (2) SF_6/C_4F_8-based inductively-coupled plasma reactive ion etching (ICP-RIE) through the silicon membrane layer, (3) removal of the electron beam resist, (4) photolithography to define a mesa stripe that intersects the electron beam defined cutouts, (5) removal of material surrounding the mesa (dry etching of the top silicon, underlying oxide, and substrate silicon layers), (6) removal of the photoresist, and (7) wet etch (hydrofluoric acid) of the underlying oxide layer to form a free-standing membrane. Figure 4.1 shows scanning electron microscope (SEM) images of fully processed devices; in addition to being isolated to the mesa stripe, additional cutout material (defined in step (1) above) surrounding each cavity has been removed to ensure that the taper interacts only with the cavity. Figure 4.2 shows close-up SEM images of a fabricated PC cavity. From these images, we can observe the quality of the dry etch processes that have been developed; the etched air holes are both smooth and vertical, each of which is necessary to achieve devices that exhibit high *Q*s.

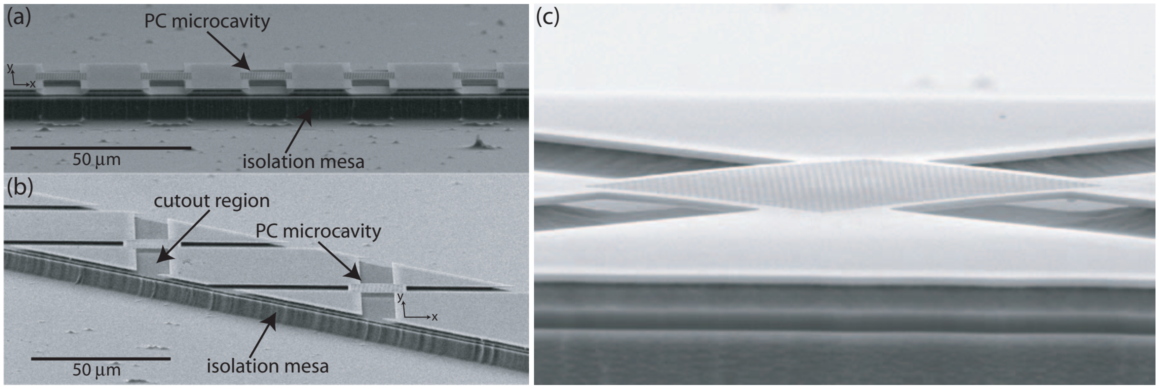

Figure 4.1: (a)-(b) Scanning electron microscope (SEM) images of photonic crystal microcavity arrays fabricated in silicon-on-insulator. The undercut PC microcavities are fabricated in a linear array that is isolated from the rest of the chip by several microns. The devices in (a) have additional material removed along the $\hat{y}$ axis of the cavity, to allow for the fiber optic taper to be aligned along that axis. The devices in (b) have additional material ('cutout region') removed along both the $\hat{x}$ and $\hat{y}$ axes, to allow probing along either axis. (c) Close-up low-angle image of a single PC cavity within the array of devices in (b).

Within the linear array of devices, we fabricate two or three different lattice constants (with a=380-430 nm, so that $a/\lambda \sim 0.25$ for λ=1600 nm, to be consistent with simulation results for the grade square lattice cavity design), and for a given a, the average hole radius ($\bar{r}/a$) is varied. The combination of varying a and $\bar{r}/a$ allows us to easily tune the cavity resonances through the range of the scanning tunable laser (λ=1565-1625 nm) that we use in our measurements.

4.3 Measurement setup

The fiber tapers we use consist of a standard single mode optical fiber (9 μm core diameter, 125 μm cladding diameter) that has been simultaneously heated and stretched down to a minimum diameter (d) on the order of the wavelength of light (λ), so that for $\lambda \sim$1.6 μm as used in our experiments, $d \sim$1-2 μm. To form the tapers used here, the heating mechanism is a hydrogen-based torch [122], but other techniques such as use of a CO_2 laser have also been studied by other groups [123]. In a taper with a suitably adiabatic transition region, the insertion loss through the taper can be quite

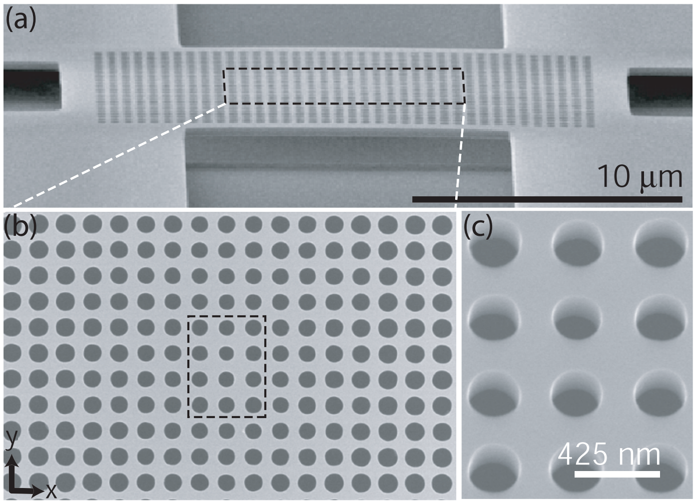

Figure 4.2: SEM micrographs of a fully fabricated PC microcavity. (a) Cross-sectional view. (b) Top view of the portion of the cavity contained within the dashed lines in (a). Total cavity dimensions are $\sim 13\mu$m $\times$ 16μm. (c) Zoomed in angled view of the dashed line region in (b) showing the smoothness and verticality of the etched air hole sidewalls, necessary to limit scattering loss and radiative coupling to TM-like modes.

low; the tapers we typically fabricate have an insertion loss of $\sim$ 10 %. The taper is mounted onto an acrylic block in a u-shaped configuration (fig. 4.3(b)), and the block is then fastened to a DC motor-controlled $\hat{z}$-axis stage with 50 nm step size resolution. Mounting the taper in this fashion naturally keeps it under tension and prevents the taper position from excessively fluctuating due to environmental factors (such as fluctuating air currents in the laboratory). The microcavity chip is in turn mounted on a DC motor-controlled $\hat{x}-\hat{y}$-axis stage with 50 nm step size resolution; in this way, the fiber taper can be precisely aligned to a microcavity. The taper-cavity interaction region is imaged with a microscope onto a CCD camera. The vertical separation between the taper and cavity can easily be calibrated by stepping the taper down in 50 nm increments until it just touches the cavity (this can be seen optically through the microscope), establishing the motor readout corresponding to a zero gap. Determining the separation in this manner is made possible by the mechanical robustness of the taper, which allows it to withstand contact to the semiconductor chip without breaking.

The mounted taper is fusion spliced into the measurement setup (fig. 4.3(a)) so that a fiber-coupled scanning tunable laser with polarization-controlling paddle wheels is connected to its input and an InGaAs photodetector measures its output. The laser and photodetector output are attached to a computer via GPIB interfaces, so that the wavelength-dependent transmission of the taper can be recorded. In addition, the motorized stages on which the taper and PC chip are mounted are also GPIB controlled, so that the taper transmission spectrum can be monitored as a function of the taper's position with respect to the cavity. When the taper is laterally aligned over the central region of the cavity and positioned vertically within the cavity's near field (typically < 1 μm), the cavity modes appear as resonances within this transmission spectrum. As we shall discuss in section 4.4, measurements of the linewidth and depth of these resonances as a function of the taper's position with respect to the cavity can give us quantitative estimates of the cavity's Q and V_{eff}.

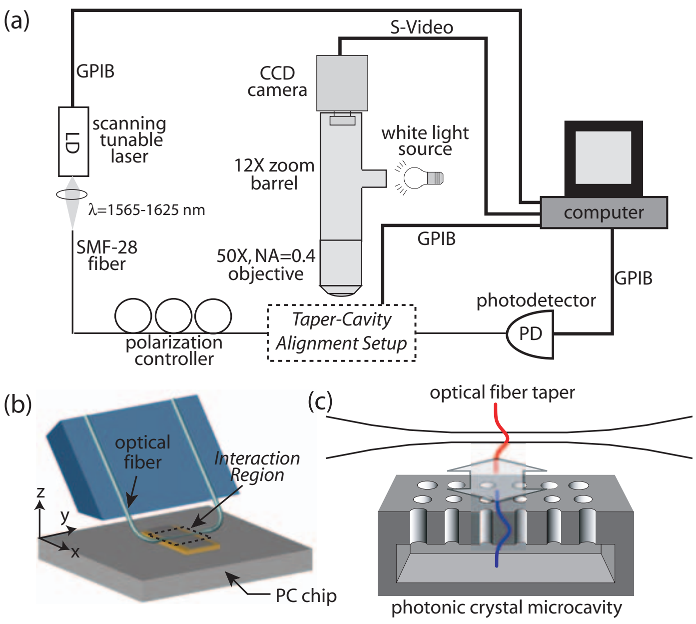

Figure 4.3: (a) Experimental measurement setup for probing optical microcavities with fiber tapers. (b) Taper-cavity alignment setup (dashed boxed region in (a)). The fiber taper is mounted in a u-shaped configuration and attached to a $\hat{z}$ axis stage with 50 nm resolution, while the underlying PC chip can be positioned in the $\hat{x}-\hat{y}$ plane with 50 nm resolution. The fiber taper is spliced into the setup in (a), which allows for measurement of its wavelength-dependent transmission spectrum. (c) Zoomed-in depiction of the taper-cavity interaction region (dashed boxed region in (b)).

In principle, the curvature of the looped taper shown in fig. 4.3(b) could be made large enough so that only a small region of the fiber interacts with the PC chip, and the taper could then be used to probe a full two-dimensional (2D) array of cavities on a chip; since the work described in this thesis was completed, Chris Michael, a student in our group, has developed a technique and fiber mounting strategy to do this. For the fiber tapers we have used in the experiments described here, however, the region of the fiber that interacts with the chip is typically around 10 mm in length, and is roughly equal to the length of the tapered region of the fiber as defined when the taper is formed. One result of this relatively long 10 mm interaction length is that testing of a 2D array is not feasible, and linear (1D) arrays of devices are tested. In addition, because coupling to the cavity requires the taper to be positioned within a micron of the center region of cavity, control of the tip and tilt of the sample with respect to the taper is necessary; this is accomplished through use of a goniometer stage mounted to the motor-controlled $\hat{x}-\hat{y}$ sample stage. Finally, to prevent the taper from interacting with extraneous portions of the chip, the cavities are isolated to a mesa stripe that is several microns above the rest of the sample surface (fig. 4.1). By appropriately angling the goniometer stage with respect to the taper, it can be ensured that when the taper is brought into contact with the chip, it only touches the cavity region.

4.4 Measurement results

The coupling between the tapered fiber waveguide and the PC microcavity can be understood using, for example, the coupling of modes in time approach as in Manolatou et al. [50]. The degree to which the taper mode couples to the cavity mode is a function of the parameter κ, which is approximately given by the field overlap between the two modes over their interaction length. More explicitly, for the taper aligned along the $\hat{y}$-axis of the cavity, it is given by:

$$\kappa = -\frac{i\omega\varepsilon_0}{4}\int_0^L e^{-i\beta y}dy\left(\iint\limits_{A_c}(n^2-n_c^2)\mathbf{E}_c^*\cdot\mathbf{E}_t dxdz + \iint\limits_{A_t}(n^2-n_t^2)\mathbf{E}_c^*\cdot\mathbf{E}_t dxdz\right), \tag{4.1}$$

where ω is the resonant cavity mode frequency, ε_0 is the permittivity of free space, β is the propagation constant of the taper mode, n is the refractive index of the background air, n_c (n_t) is the refractive index profile of the cavity (taper), $\mathbf{E}_c$ ($\mathbf{E}_t$) is the electric field vector of the cavity (taper), L is the interaction length of the coupling, and the integrals over A_c and A_t are two-dimensional integrals over the x-z cross section within the cavity and taper, respectively, for a given y value within the interaction length. From this formula, we see that κ is dependent upon: (i) the magnitude of the overlap between $\mathbf{E}_c$ and $\mathbf{E}_t$, (ii) the relative phase between $\mathbf{E}_c$ and $\mathbf{E}_t$, and (iii) the degree to which $\mathbf{E}_c$ and $\mathbf{E}_t$ share a common direction of polarization.

4.4.1 Polarization

Considering the latter point, for the taper aligned along the $\hat{y}$-axis of the cavity, as in fig. 4.4(a), the polarization-controlling paddle wheels are used to select a linearly polarized state of the taper whose dominant field component is aligned along the $\hat{x}$-axis of the cavity. Thus, modes that couple most strongly will have their $\hat{x}$ field component overlap strongly with the $\hat{x}$ component of the taper field. By aligning the taper along a different axis of the cavity, polarization selectivity can be realized. For the devices in Figs. 4.1(a) and 4.4(a), this is not possible, as aligning the taper along the $\hat{x}$-axis will couple the taper to multiple cavities. However, by fabricating the cavities at a 45° angle with

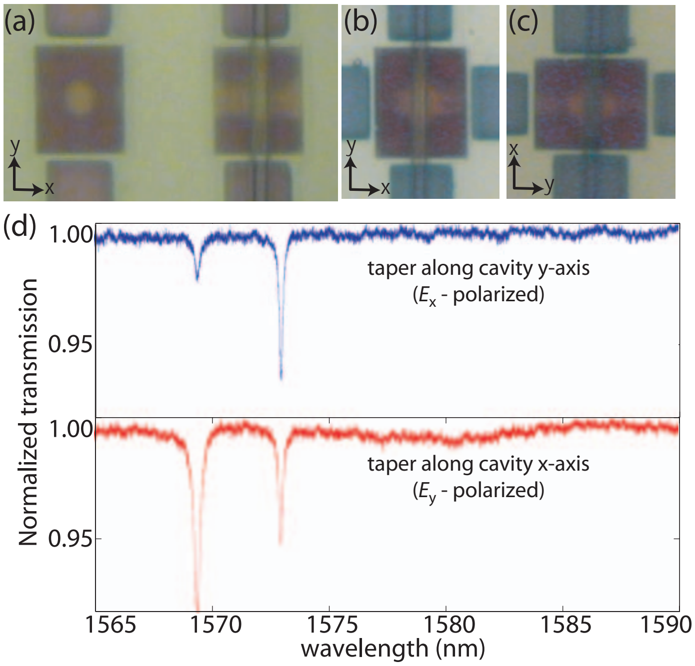

Figure 4.4: (a)-(c) Optical micrograph image of a fiber taper aligned along (a) the $\hat{y}$-axis of one of the cavities from fig. 4.1(a); (b)-(c) the $\hat{y}$ and $\hat{x}$ axes, respectively, of one of the cavities from fig. 4.1(b). (d) Normalized taper transmission when the taper is ~ 350 nm above a PC cavity of the type shown in fig. 4.1(b); (top) Taper aligned along the cavity's $\hat{y}$-axis (bottom) Taper aligned along the cavity's $\hat{x}$-axis.

respect to the isolation mesa stripe, as in fig. 4.1(b), the taper can be aligned along either of the orthogonal cavity axes without coupling to multiple devices. In fig. 4.4(b)-(c), we show the optical fiber taper aligned parallel to the $\hat{y}$ and $\hat{x}$ axes of one of the cavities from fig. 4.1(b). When the taper is laterally aligned with the center of the cavity and brought vertically close to it, we observe the cavity's resonances. As shown in fig. 4.4(d), the coupling is polarization selective, so that those resonances with dominant cavity field component E_x couple most strongly when the taper is aligned along the $\hat{y}$-axis of the cavity (fig. 4.4(b)), while those with dominant cavity component E_y couple most strongly when the taper is aligned along the cavity's $\hat{x}$-axis (fig. 4.4(c)). Thus, the shorter wavelength resonance in fig. 4.4(d) is more strongly polarized along the $\hat{y}$-axis, while the longer wavelength resonance is more strongly polarized along the $\hat{x}$-axis. This data is consistent with simulation and group theoretical results that predict that these square lattice microcavities support modes of types A_2 and B_2 symmetry, which are predominantly polarized along the $\hat{x}$ and $\hat{y}$ axes of the cavity, respectively [21]. The coupling depths of a few percent are typical values, and were found to be adequate to achieve a sufficient signal-to-noise ratio for all of the measurements presented in the upcoming sections.

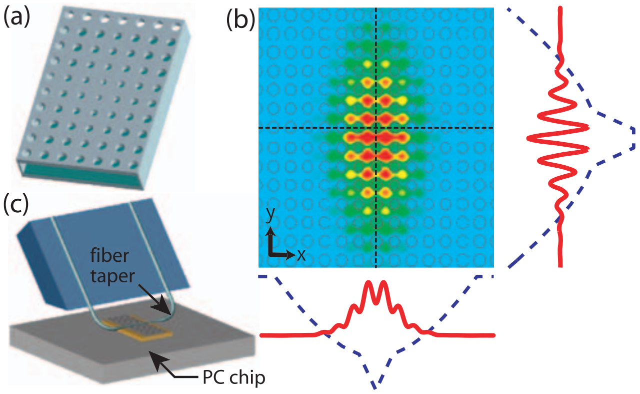

Figure 4.5: Summary of the design of the graded square lattice photonic crystal microcavity. (a) Schematic of the undercut, two-dimensional PC microcavity geometry. (b) Magnetic field amplitude ($|\mathbf{B}|$) in the center of the PC membrane for the A_2^0 mode. The dashed curves show the grade in hole radius (r/a) along the central $\hat{x}$ and $\hat{y}$ axes of the cavity (marked by dashed lines through the dielectric lattice), and the solid curves are slices of the field component B_z along these directions.

4.4.2 High-Q measurements

For future microcavity-enhanced experiments within our graded square lattice PC geometry, the fundamental TE-like mode of A_2 symmetry, which we label as the A_2^0 mode, is of particular interest, on account of its predicted ultrasmall V_{eff} and high Q factor. Let us briefly review some of the key features of this mode: the PC cavity geometry employed is shown in fig. 4.5(a-b), and was designed using group theoretical, Fourier space, and finite-difference time-domain (FDTD) analyses as described in detail in chapter 2. The cavity consists of a localized defect in a square lattice of air holes that are etched into an optically thin membrane of refractive index n=3.4. This geometry provides in-plane modal localization via distributed Bragg reflection due to the lattice and vertical confinement by total internal reflection at the membrane-air interface. The resulting TE-like A_2^0 defect mode shown in fig. 4.5(b) is predicted to have $Q \sim 10^5$ and $V_{\text{eff}} \sim 1.23\ (\lambda_c/n)^3$. The important aspects of the cavity design are: (1) the dominant electric field component, E_x, is odd about the $\hat{x}$-axis, thereby reducing vertical radiation loss from the patterned slab, (2) a grade in the hole radius is used to both further confine the mode in-plane and reduce in-plane radiative losses, and (3) the design is relatively insensitive to perturbations to the cavity, as verified through simulations where the steepness of the grade and the average hole radius ($\overline{r}$) have been varied significantly without degrading the Q below $\sim 20,000$.

To experimentally locate a device for which this mode appears within the scan range of the laser we use (1565-1625 nm), we rely on the fact that it is the fundamental (and hence lowest frequency) mode within the region of $\omega - k$ space under consideration. In particular, for a given lattice constant a, we begin testing by examining the device with the largest $\overline{r}/a$. Typically, the

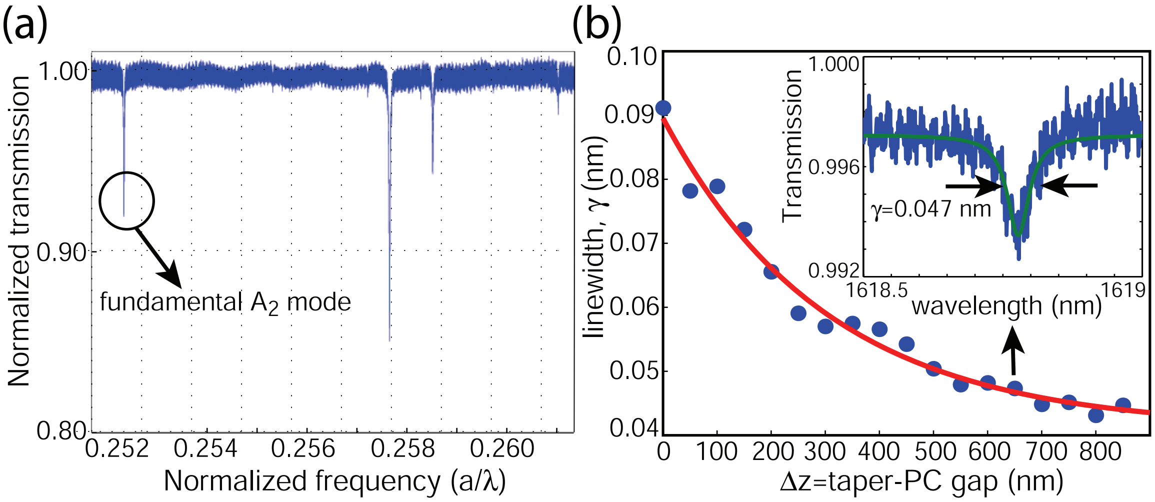

Figure 4.6: Fiber taper transmission measurements of the PC microcavities. (a) Taper transmission spectrum for a cavity with a=409 nm, where the data has been normalized to a background spectrum when the taper is far above the cavity. The highlighted long wavelength mode is the A_2^0 resonant mode. (b) Measured linewidth (dots) versus taper-cavity gap (Δz) for the A_2^0 mode ($a/\lambda_c \sim 0.263$) in a sample with a=425 nm. The taper is vertically positioned by a stepper motor with 50 nm encoder resolution. The solid curve is a fit to the experimental data. (inset) Normalized taper transmission versus wavelength when the taper is 650 nm above the cavity surface.

resonances of this device are at frequencies that are above that covered by the laser scan range, and hence, no resonances are observed in the taper's transmission spectrum. We then move on and test the next device in the array, which has a slightly smaller $\bar{r}/a$ and is thus predicted to have lower frequency resonances than the previous device. This process is continued until we find a device for which a resonance is seen in the transmission spectrum. The first resonance which appears in the transmission spectrum (measuring from lowest frequency to highest frequency) is the A_2^0 mode; this identification procedure relies on having only small changes in $\bar{r}/a$ between successive devices in the array, so that the cavity resonances can be smoothly tuned from frequencies above the laser scan range to frequencies within the scan range. However, this identification of the A_2^0 mode can be confirmed, both by comparing the measured resonance frequency with that predicted from FDTD simulations using the SEM-measured hole sizes, and as discussed later, by comparing the spatial localization of the cavity mode with that predicted from simulations. In addition, as described in the previous section, the polarization of the input light into the taper can be used to rule out modes that are not of the correct polarization.

Having identified a device for which the A_2^0 mode appears within the scan range of the laser (fig. 4.6(a)), we next examine its Q factor. In the inset of fig. 4.6(b), we show a wavelength scan of the taper transmission showing the resonance dip of the A_2^0 mode for a device within the array shown in fig. 4.1(b), where the vertical taper-cavity separation Δz=650 nm. An initial estimate of the Q of this resonance (centered at wavelength λ_0) is given by measuring its linewidth γ, with $Q = \lambda_0/\gamma$. For this device, $\lambda_0 \sim 1618.75$ nm and $\gamma \sim 0.047$ nm (where these values are determined by fitting the data to a Lorentzian curve), giving an estimate of $Q \sim 34,400$. This Q is a lower bound for the cold-cavity Q, due to the taper's loading effects on the cavity, which cause its linewidth to broaden. Loading by the taper results in out-coupling to the *forward* propagating fundamental taper mode which, upon interference with the power directly transmitted past the cavity, results in the observed resonant feature in the taper transmission. Parasitic taper loading effects could include coupling to radiation modes, higher-order taper modes, and the *backward* propagating fundamental taper mode. To estimate the taper loading effects on the A_2^0 cavity mode, we examine γ as a function of Δz. The resulting data (fig. 4.6(b)) shows that as Δz increases, the loading effects are reduced, until a regime is reached where the taper does not significantly affect the cavity mode and the measured linewidth asymptotically approaches the cold-cavity linewidth. Assuming that the loading is monoexponentially related to Δz, we fit the measured linewidth to the function $\gamma = \gamma_0 + \beta e^{-\alpha \Delta z}$, where γ_0, β, and α are all fitting parameters. The resulting fit value of γ_0 is 0.041 nm, essentially identical to the directly measured linewidth when $\Delta z \gtrsim 800$ nm, and corresponds to a cold-cavity $Q \sim 39,500$.[1] To compare this result directly with numerical calculations, we repeat our previous FDTD calculations from chapter 2 but include an offset in $\bar{r}$ of $r/a = 0.05$ to account for the increased size of the fabricated holes (as measured by SEM) relative to the design of fig. 4.5. Doing so yields a predicted $Q \sim 56,000$ and $a/\lambda_c \sim 0.266$, fairly close to the measured values, and $V_{\text{eff}} = 0.88(\lambda_c/n)^3$, smaller than the original design due to the better in-plane confinement provided by the larger hole radii.

4.4.3 Spatial localization measurements

As mentioned earlier, the extremely small volumes to which light is confined within PC microcavities is one of their distinguishing advantages over other optical microcavities, and is of critical importance in many applications, as the per photon electric field strength within the cavity is proportional to $1/\sqrt{V_{\text{eff}}}$. The ability to experimentally confirm such tight spatial localization using the same probe that maps the spectral properties (such as the Q) of the cavity modes is an important

---

[1] Note that some parasitic taper loading effects may not diminish as a function of Δz as rapidly as does the coupling between the fundamental taper mode and cavity mode of interest. This could prevent the measured linewidth γ from reaching an asymptotic value as a function of Δz. In such cases, the best estimate of γ_0 is the linewidth for as large a Δz as can be reliably measured.

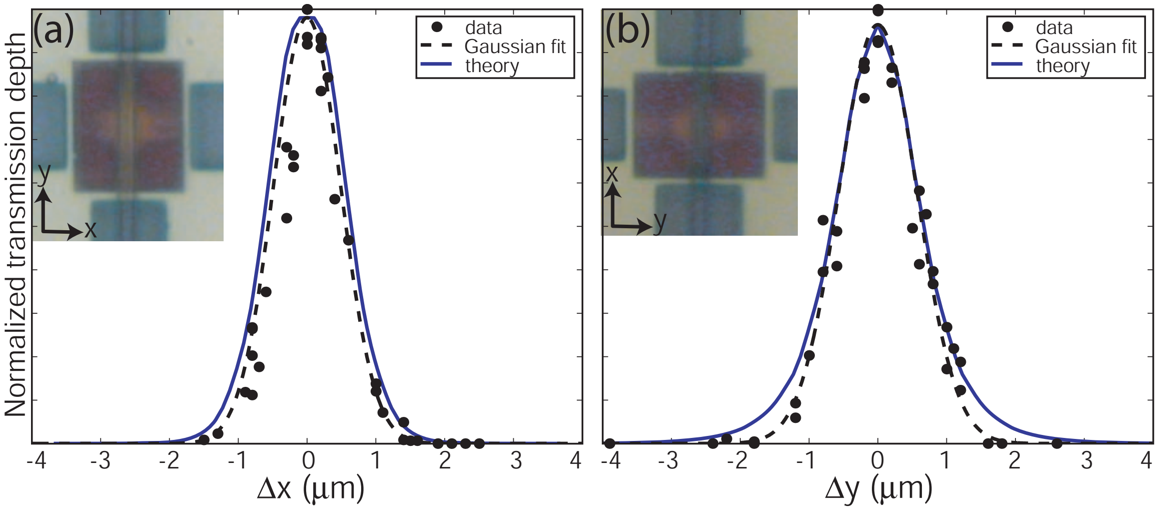

Figure 4.7: Mode localization data for the cavity whose Q was measured in fig. 4.6. The measured normalized taper transmission depth (black dots) is plotted as a function of taper displacement along the (a) $\hat{x}$-axis and (b) $\hat{y}$-axis of the cavity. The dashed line in (a)-(b) is a Gaussian fit to the data while the solid line is a numerically calculated coupling curve based upon the FDTD-generated cavity field and analytically determined fundamental fiber taper mode (taper diameter $d \sim 1.7$ μm)

.

demonstration of the versatility of the optical fiber taper. Here, the same near field probe is used to both excite the PC cavity modes and to map their spatial profile. Other works employing evanescent coupling from eroded monomode fibers to excite silica microsphere whispering gallery modes have used a secondary fiber tip to collect and map the mode profiles [124].

The spatial localization of the cavity mode is easily probed by examining the strength of coupling between it and the taper as the taper is laterally scanned above the surface of the cavity. The strength of coupling is reflected in the depth of the resonant dip in the taper transmission.[2] In the insets of fig. 4.7(a)-(b), we show the fiber taper aligned along the $\hat{y}$ and $\hat{x}$-axis of the photonic crystal microcavity whose Q was measured to be $\sim 40,000$. The position of the taper is varied along the $\hat{x}$ and $\hat{y}$ axes of the cavity (at a fixed vertical taper-PC gap $\Delta z = 200$ nm), respectively, allowing for measurements of the depth of coupling along these two orthogonal cavity directions. The depth of the resonant transmission dip for the A_2^0 cavity mode versus taper displacement is shown in Figs. 4.7(a) and 4.7(b), respectively. These measurements show the mode to be well localized to a micron-scale central region of the cavity, giving experimental confirmation that the A_2^0 mode of this cavity is both high-Q and small V_{eff}. As might be expected, they do not reveal the highly

---

[2] The maximum transmission depth achieved for the mode of interest was $\sim 10\%$, though coupling to other modes reached depths as large as $\sim 30\%$. Coupling in all cases was limited to the *under-coupled* regime [125, 20].

oscillatory cavity near field, but instead an envelope of the field, due to the relatively broad taper field profile. To compare this experimental data with FDTD calculations, we consider a simple picture of waveguide-cavity coupling [50], where the coupling coefficient (κ) is approximated, to save computation time, by taking the field overlap of the phase matched Fourier components of the FDTD-generated cavity field with the analytically-determined taper field (the modes of a cylindrical dielectric waveguide are derived in ref. [126], for example). The calculated resonant transmission depth as a function of taper displacement is shown in Figs. 4.7(a)-(b) as a solid line and agrees closely with the measured data, providing further confirmation that the mode studied is indeed the A_2^0 mode of interest. Assuming that the cavity mode is localized to the slab in the $\hat{z}$-direction (a good assumption based upon measurements that show the depth of coupling between the taper and cavity mode decreases exponentially as the taper-cavity separation is increased), the close correspondence between the measured and calculated in-plane localization indicates that $V_{\text{eff}} \sim 0.9(\lambda_c/n)^3$ for this high-Q mode, where this V_{eff} value was calculated through FDTD simulations which take into account the SEM-measured hole radii for this device.

Similar measurements of the higher-frequency resonant modes of the PC microcavity indicate that they are more delocalized in-plane in comparison to the A_2^0 mode, and sometimes contain multiple lobes within their coupling curves, as one might expect for higher-order modes of the cavity. As an example of this, we show in fig. 4.8(a)-(b) the depth of coupling to a higher order mode as a function of the taper's position along the $\hat{x}$ and $\hat{y}$ axes of the cavity, respectively. The node that appears within the coupling curve in fig. 4.8(a) results from the cavity and taper modes being precisely out of phase so that the integral determining κ in equation 4.1 is zero, and is a result of the measurement being sensitive to the fields within the cavity and taper rather than their intensities. These results indicate that the mode is likely fundamental along the $\hat{y}$-axis (its width is close to that measured in fig. 4.7(b)), while it is a higher order mode along the $\hat{x}$-axis. Simulations confirm that such modes are supported by the graded lattice geometry employed in this work.

With the exception of such cases where there is phase cancelation in κ, the resolution of the fiber taper probe is limited by the transverse profile of the taper mode. This is the reason why the measured coupling curves give an envelope of the cavity field rather than displaying its oscillatory nature; in the measurements of fig. 4.7, for example, the calculated full width at half maximum (FWHM) of the dominant taper field component at the center of the PC slab is $\sim \lambda_0$, while the cavity mode oscillates on the scale of a lattice constant a (fig. 4.5(b)), and $a/\lambda_0 \sim 0.25$. The taper used in these measurements had a diameter $d \sim 1.7$ μm ($d/(\lambda_0/n) \sim 1.52$, where $n \sim 1.45$ is

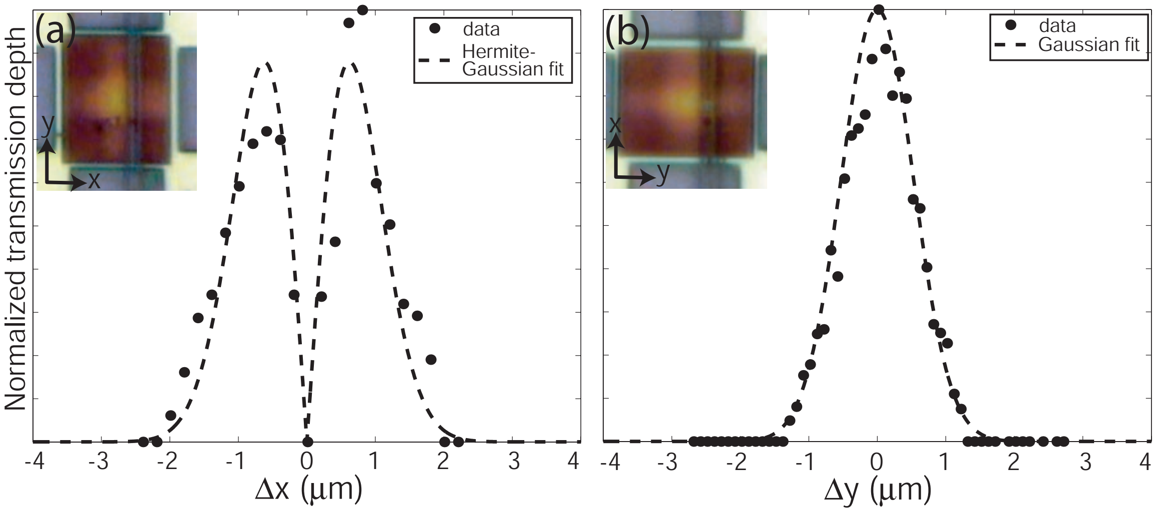

Figure 4.8: Mode localization data for a higher order mode of the graded square lattice PC cavity. The measured normalized taper transmission depth (black dots) is plotted as a function of taper displacement along the (a) $\hat{x}$-axis and (b) $\hat{y}$-axis of the cavity. The dashed line in (a) is a Hermite-Gaussian fit to the data and the dashed line in (b) is a Gaussian fit to the data.

the refractive index of the silica taper), and intuitively, it might be expected that better resolution could be achieved by further reducing its diameter. However, for the relatively small taper diameters ($\sim \lambda_0$) with which we operate, we note that the waveguiding properties of the taper begin to degrade below some minimum diameter so that, even if a smaller taper is used, it does not necessarily confine the mode any more tightly than a larger taper would.[3] To better illustrate this, in fig. 4.9, we plot the calculated normalized FWHM of the dominant taper field component at the center of the PC slab for varying normalized taper diameter ($d/(\lambda_0/n)$) and taper-PC slab separation ($\Delta z/\lambda_0$). As expected, the smallest FWHM$\sim 1.23(\lambda_0/n)$ occurs when $\Delta z/\lambda_0$=0, that is, when the taper is touching the slab.[4] We also see that reducing $d/(\lambda_0/n)$ below some minimum value begins to broaden the FWHM. Thus, for the spatial localization measurements, using smaller tapers will not appreciably improve the resolution of the measurement. Possibilities for future improvement might consist of partially aperturing the taper field (perhaps through a metallic coating on the taper), or forming the waveguide probe from a higher index material. As it stands with the current silica taper used, the width of the taper mode will limit the degree to which cavity modes of differing

---

[3] This simple point is very important when trying to compare the modal confinement properties of sub-micron diameter silica waveguides, now commonly called nanowire waveguides, with those of high-index contrast waveguides like PCs.

[4] In practice, a non-zero Δz, on the order of $\sim$ 250 nm for λ_0=1.6 μm, is preferable for doing spatial localization measurements. This is due both to the relatively large amount of insertion loss that occurs when the taper touches the cavity, and also to allow the taper to be freely moved above the cavity.

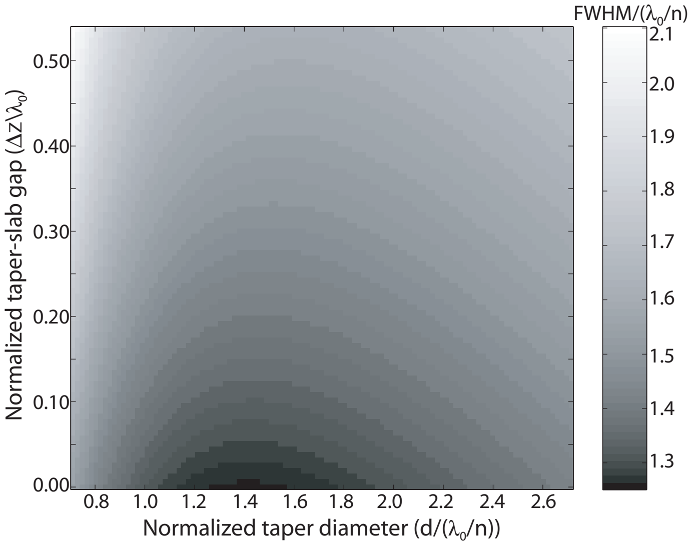

Figure 4.9: Resolution of the fiber taper. Plot of the normalized full-width at half-maximum (FWHM/(λ_0/n)) of the dominant taper electric field component at the center of the PC slab, as a function of normalized taper-slab gap ($\Delta z/\lambda_0$) and taper diameter ($d/(\lambda_0/n)$). λ_0 is the operating wavelength of the taper (and the resonant frequency of the cavity mode), and $n \sim 1.45$ is its material refractive index.

spatial localizations can be distinguished (differences in cavity localization will be blended out in the measured coupling curves, due to the effect of the convolution with the taper field). Nevertheless, we have been able to distinguish modes with localizations corresponding to differences in V_{eff} of $\sim 0.3(\lambda/n)^3$ in our work to this point.

4.5 Applications to quantum optics

To illustrate the potential applications of such a small V_{eff} and high-Q microcavity, we briefly consider two examples from quantum optics. The Purcell factor (F_P), a measure of the microcavity-enhanced spontaneous emission rate of an embedded active material, is given under suitable (maximal) conditions as (see appendix H and ref. [109]):

$$F_P = \frac{3}{4\pi^2}\left(\frac{\lambda_c}{n}\right)^3\left(\frac{Q}{V_{\text{eff}}}\right). \tag{4.2}$$

For the A_2^0 mode ($Q \sim 40,000$, $V_{\text{eff}} \sim 0.9(\lambda_c/n)^3$), the predicted F_P is $\sim 3,500$, an extremely large value for a semiconductor-based microcavity (previous work on semiconductor microdisks [13] have predicted $F_P \sim 190$, for example).

Another application is in cQED, where strongly coupled atom-photon systems have been proposed as candidates to produce the quantum states required for quantum computing applications [60]. For such applications, the regime of strong coupling (see Appendices G-H and ref. [9]), where the atom-photon coupling coefficient (g) exceeds the cavity and atomic decay rates (κ and $\gamma_{\perp}$, respectively), must be reached. Although strong coupling has been achieved in systems consisting of an alkali atom and an actively stabilized Fabry-Perot cavity [9], in future applications, where higher levels of integration are sought, chip-based cavities are of interest [60]. Using the measured Q and estimated V_{eff} for the A_2^0 mode studied here, the relevant parameters for a commonly-used Cesium (Cs) atomic transition ($\lambda_0 = 852$ nm, $\gamma_{\perp}/2\pi = 2.6$ MHz) [9], and the formulas (see appendix H)

$$\begin{aligned} g &= \eta\gamma_{\perp}\sqrt{\frac{3c\lambda_0^2}{4\pi\gamma_{\perp}V_{\text{eff}}}} \\ \kappa &= \frac{\omega}{2Q} \end{aligned} \tag{4.3}$$

we calculate $g/2\pi \sim 16$ GHz and $\kappa/2\pi \sim 4.4$ GHz, indicating that the coupled Cs-PC cavity system could achieve strong coupling.[5] In addition, the calculated critical atom number ($N_0 = 2\kappa\gamma_{\perp}/g^2$) and saturation photon number ($m_0 = \gamma_{\perp}^2/2g^2$) are $N_0 \sim 8.8\text{x}10^{-5}$ and $m_0 \sim 1.3\text{x}10^{-8}$, a regime where a single atom would have a profound effect on the cavity field, and vice versa. More detailed calculations using the optical bistability state equation and quantum master equation have been performed [62], and confirm that it should be possible to detect single strongly coupled atoms in this system. Such experiments are being explored by Paul Barclay and Ben Lev in a collaborative effort between the Mabuchi and Painter groups at Caltech. In addition, calculations of the coupling and decay parameters for an InAs semiconductor quantum dot [127] indicate that the current PC microcavity would also be capable of reaching strong coupling in such a solid-state system. Calculations based on the quantum master equation are the focus of chapter 8, and so I will refrain from adding anything more on this here.

4.6 Fabrication-tolerant high-Q cavities

In this section, we investigate the robustness of the Q of the A_2^0 mode in our PC cavity design to imperfections in the lattice. The basic motivation for this work has been the observation that many fabricated PC cavities exhibited Q factors that were significantly smaller than the values expected from simulations. In some cases, this may have been due to issues such as surface state or bulk

---

[5] As V_{eff} is defined relative to peak electric field energy density, rather than electric field strength, a factor η must be included in g for dielectric cavities where the two values are not equal. $\eta \sim 0.42$ for our cavity.

material absorption, or due to problems with the etch used, resulting in angled sidewalls or rough etched surfaces. The robustness I study in this chapter does not cover such instances. Here, I focus purely on the response of the Q to variations in the size of the holes within the PC lattice. Although covering only one subset of the imperfections that can occur during fabrication, it is an important subset, as it is directly related to processes such as electron beam lithography, where incorrectly sized holes can result from variations in the beam current during the writing step, and plasma dry etching, where etches can undercut the mask and lead to larger holes than what were intended.

A range of designs have been employed in studies of high-Q PC microcavities [11, 21, 26, 51], and in many cases, the experimental achievement of high-Q is predicated on the ability to fabricate the design with a small margin for error. For example, in ref. [12], the discrepancy between the fabricated device and the intended design led to a theoretical degradation of Q from 3.0×10^4 to 4.4×10^3, close to the measured Q of 2.8×10^3. Extraordinary control over fabricated geometries has been demonstrated in recent work [51], where a shift of ~ 60 nm in the positions of holes surrounding the cavity defect region reduced Qs as high as 4.5×10^4 by over an order of magnitude. Here, we discuss a study of our PC microcavity design (chapter 2), which exhibits a degree of robustness, both theoretically and experimentally, to deviations from the nominal design sufficient for Qs above 10^4 to be maintained. This robustness in Q to changes in the PC cavity geometry is of practical importance for future experiments, to provide insensitivity to fabrication imperfections, as well as to maintain the flexibility in cavity design required to form resonant modes with a prescribed field pattern and polarization.

Radiative losses in planar waveguide PC defect microcavities can be separated into in-plane and out-of-plane components, quantified by the quality factors $Q_{\parallel}$ and $Q_{\perp}$, respectively, with the total radiative Q given by $Q^{-1} = Q_{\parallel}^{-1} + Q_{\perp}^{-1}$. $Q_{\parallel}$ is determined by the size and angular extent (in-plane) of the photonic bandgap, while $Q_{\perp}$ is determined by the presence of in-plane momentum components ($\mathbf{k}$) within the waveguide cladding light cone, which are not confined by total internal reflection at the core-cladding interface. In chapter 2 and ref. [21], PC microcavities were designed using two mechanisms to avoid radiative loss: (i) use of a mode that is odd about mirror planes normal to its dominant Fourier components, in order to eliminate the DC ($\mathbf{k} = \mathbf{0}$) part of the in-plane spatial frequency spectrum and hence reduce vertical radiation loss, and (ii) use of a grade in the hole radius to further confine the mode and reduce in-plane radiative losses. The resulting PC microcavity design within the square lattice creates a TE-like donor-type defect mode (labeled A_2^0), as shown in fig. 4.5. FDTD simulations of this resonant mode predict a Q-factor of 10^5 and an effective modal volume of $V_{\text{eff}} \sim 1.2(\lambda/n)^3$. We now show how use of mechanisms (i) and (ii) above create a level of robustness in the cavity design.

Use of an odd symmetry mode to suppress vertical radiation loss is, at a basic level, independent of changes in the size of the holes defining the defect cavity. This feature has been confirmed in the simulations of simple defect cavity designs in square lattice photonic crystals in chapter 2, where $Q_{\perp}$ did not degrade below 10^4, despite significant changes (as much as 40%) in the size of the (two) central defect holes. Perturbations that cause the cavity to be asymmetric create a mode which, though not strictly odd, will be a perturbation to an odd mode, and hence will still largely suppress DC Fourier components and exhibit high Q. However, for the square lattice photonic crystal structures considered here, perturbations to the central defect hole geometry can result in a degradation in $Q_{\parallel}$, due in part to the lack of a complete in-plane bandgap within the square lattice. This lack of a complete bandgap requires the defect geometry to be tailored so as to eliminate the presence of Fourier components in directions where the lattice is no longer reflective.

This tailoring was achieved in chapter 2 by a grade in the hole radius moving from the center of the cavity outwards. The grade, shown in fig. 4.5, serves to help eliminate couplings to in-plane radiation modes along the diagonal axes of the square lattice (the M-point of the reciprocal lattice) where the PC is no longer highly reflective, while simultaneously providing a means to keep the in-plane reflectivity high along the $\hat{y}$ axis (the direction of the mode's dominant Fourier components). The use of a large number of holes to define the defect region ensures that no single hole is responsible for creating the potential well that confines the resonant mode, making the design less susceptible to fluctuations in the size of individual holes. Instead, the continuous change in the position of the conduction band edge resulting from the grade in hole radius creates an approximately harmonic potential well [25]. This smooth change in the position of the band edge creates a robust way to mode match between the central portion of the cavity (where the mode sits) and its exterior. In other work [51], softening of this transition is achieved by adjusting the position of two holes surrounding the central cavity region (which consists of three removed air holes in a hexagonal lattice). This method can achieve high-Q, but as mode-matching is achieved by tailoring only two holes it is more sensitive to perturbations than the adiabatic transition created by a grade in the hole radius. Finally, we note that even though a relatively large number of holes are modified to create the graded lattice, V_{eff} is *still* wavelength-scale, and remains between $0.8\text{-}1.4(\lambda/n)^3$ in all of the devices considered in this work. In addition, the methods used here to achieve robustness in Q are general and can be applied to cavities in other PC lattices [23].

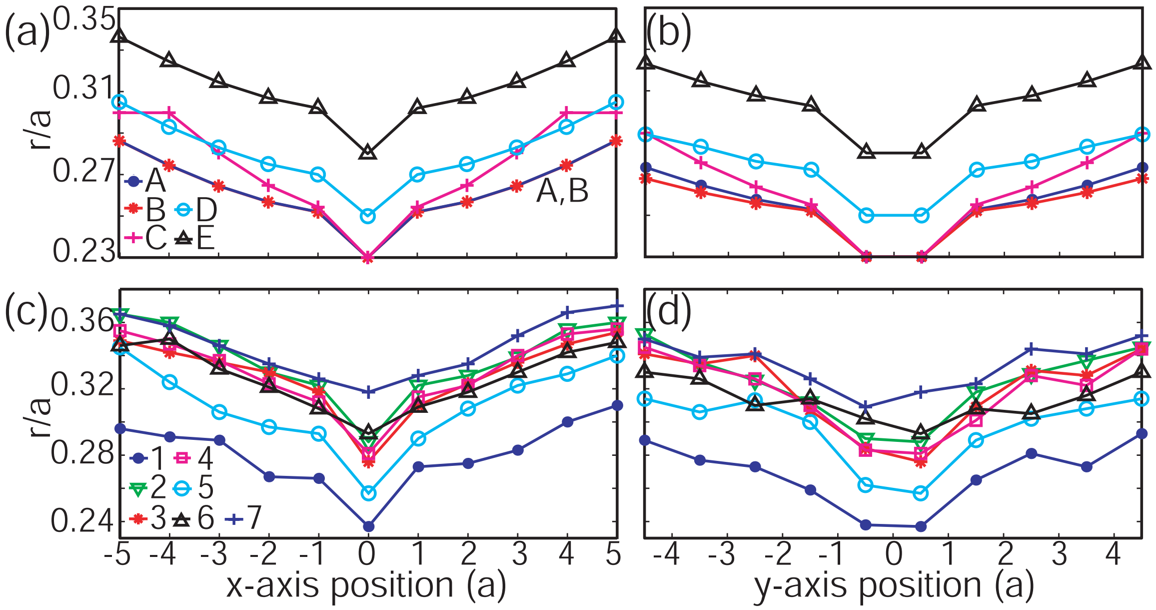

Figure 4.10: Grade in the normalized hole radius (r/a) along the central $\hat{x}$ and $\hat{y}$ axes of square lattice PC cavities. Cavity r/a profiles for (a,b) FDTD cavity designs and (c,d) microfabricated Si cavities.

To highlight these ideas, 3D FDTD simulations of cavities with varying grades and average normalized hole radius ($\overline{r}/a$) were performed. Figure 4.10(a)-(b) shows the grade in r/a along the central $\hat{x}$ and $\hat{y}$ axes for several designs (PC-A through PC-E), and table 4.1 lists the calculated resonant frequency, vertical, in-plane, and total Q factors. In all of these simulations, $Q_{\perp}$ remains close to 10^5, with PC-E showing more significant degradation largely as a result of the increased modal frequency (creating a larger-sized cladding light cone). In addition, an inappropriate choice of grade along the $\hat{x}$-axis can lead to increased in-plane losses via coupling to M-point modes. Nevertheless, the loss in any of the simulated devices did not cause Q to be reduced below 2×10^4.

To test the sensitivity of the design to perturbations experimentally, cavities were fabricated in a d=340 nm thick silicon membrane through a combination of electron beam lithography, inductively-coupled plasma reactive ion etching, and wet etching. Figure 4.10(c)-(d) shows the values of r/a along the central $\hat{x}$ and $\hat{y}$ axes for a number of fabricated devices (PC-1 through PC-7), as measured with a SEM. Cavities are passively tested using the optical fiber taper probing method described in the previous sections.

Figure 4.11(a)-(b) shows measurements for devices PC-5 and PC-6, which have significantly different r/a profiles (fig. 4.10(c)-(d)). The inset of fig. 4.11(c) shows the normalized taper trans-

Table 4.1: Theoretical (PC-A through PC-E) and experimental (PC-1 through PC-7) normalized frequency (a/λ_o) and quality factor (Q) values for the A_2^0 mode of cavities with r/a profiles shown in fig. 4.10.

Cavity	d/a	a/λ_0	$Q_\perp$	$Q_\parallel$	Q
PC-A	0.750	0.245	1.1×10^5	4.7×10^5	9.0×10^4
PC-B	0.750	0.245	1.1×10^5	2.6×10^5	7.5×10^4
PC-C	0.750	0.247	1.0×10^5	3.7×10^5	8.0×10^4
PC-D	0.750	0.253	8.6×10^4	3.0×10^5	6.7×10^4
PC-E	0.750	0.266	6.2×10^4	6.5×10^5	5.6×10^4
PC-1	0.879	0.241	-	-	1.6×10^4
PC-2	0.850	0.255	-	-	1.8×10^4
PC-3	0.850	0.251	-	-	1.7×10^4
PC-4	0.842	0.251	-	-	2.4×10^4
PC-5	0.842	0.249	-	-	2.5×10^4
PC-6	0.800	0.263	-	-	4.0×10^4
PC-7	0.800	0.270	-	-	1.3×10^4

mission as a function of wavelength when the taper is 350 nm above cavity PC-5. By measuring the dependence of cavity mode linewidth (γ) on the vertical taper-PC gap (Δz) (fig. 4.11(a)), an estimate of the true cold-cavity linewidth (γ_0) is given by the asymptotic value of γ reached when the taper is far from the cavity. For PC-5, $\gamma_0 \sim 0.065$ nm, corresponding to $Q \sim 2.5\times10^4$. Figure 4.11(b) shows the linewidth measurement for PC-6. For this device, $\gamma_0 \sim 0.041$ nm, corresponding to a $Q \sim 4.0\times10^4$.

Linewidth measurements for each of the cavities PC-1 through PC-7 are compiled in table 4.1. The robustness of the Q to non-idealities in fabrication is clearly evident. Though all of the devices exhibit a general grade in r/a, the steepness of the grade and the average hole radius ($\bar{r}/a$) vary considerably without reducing Q below 1.3×10^4. These high-Q values are exhibited despite the fact that many cavities are not symmetric (the odd boundary condition is thus only approximately maintained), and the frequency of the cavity resonance varies over a 10% range, between $a/\lambda_o =$ 0.243-0.270.

The measured Q values in table 4.1 are still lower than predicted from simulations. This discrepancy is likely due in part to slightly angled etched sidewalls that have been shown in calculations to lead to radiative coupling to TM-like modes [114]. This non-ideality helps explain why PC-1,

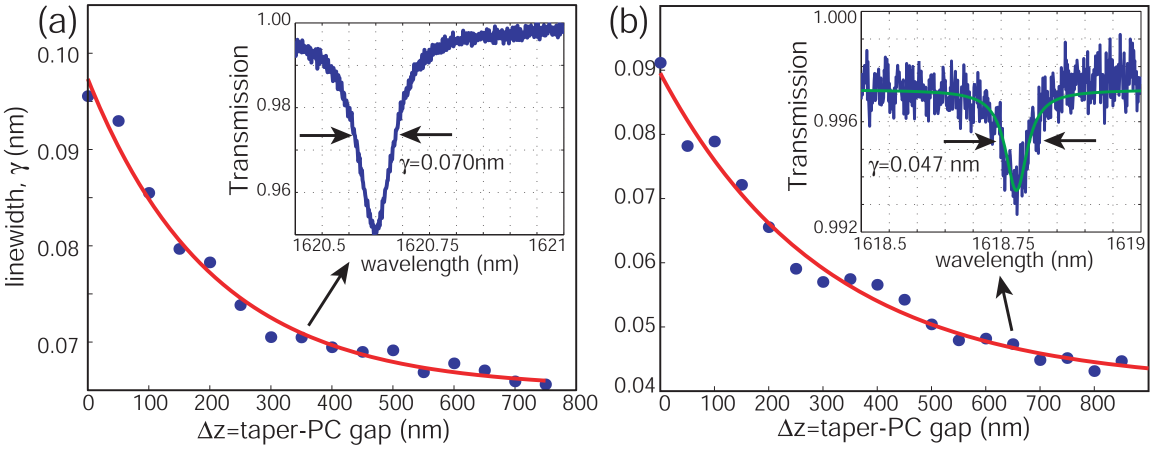

Figure 4.11: (a) Measured data (blue dots) and exponential fit (red curve) for linewidth vs. taper-PC gap of the A_2^0 mode in PC-5. (Inset) Taper transmission for this device when the taper-PC gap is 350 nm. (b) Same as (c) for PC-6 (here, the taper transmission in the inset is shown when Δz=650 nm). The transmission curves are normalized relative to transmission in the absence of the PC cavity.

which is closest in r/a value to the desired design (PC-A), does not exhibit the highest Q experimentally. In particular, we have observed that the sidewall angle is poorer for smaller sized holes. On the other end of the spectrum, cavities with the largest hole sizes such as PC-7, which may have more vertical sidewalls, also begin to exhibit higher vertical radiation loss as a result of a larger modal frequency and cladding light cone. In addition, surface roughness is a potential source of loss; for PC-6, which exhibited the highest Q value, a chemical resist stripping process was used (rather than a plasma descum) and may have produced a cleaner, smoother surface. More recently, work on Si microdisk cavities [128] has indicated that absorption due to surface layers may be a limitation. Proper termination of etched surfaces is an important consideration for achieving higher Qs in these devices.

4.7 Fiber tapers as an optical probe for photonic crystal microcavities

The versatility of the optical fiber taper measurement technique has led us to think of it as a probe for studying the properties of microphotonic structures. In this section, we further elaborate on this idea, by comparing this method to some of the existing ways in which PC microcavities (and wavelength-scale semiconductor microcavities in general) are tested.

In general, measurements of PC microcavities are not necessarily straightforward, in large part due to their micron-scale V_{eff} values, which limit the ability to effectively couple to them from free-space or through prism-based techniques, as can be done for larger microresonators such as Fabry-Perot cavities [9] and microspheres [129]. This difficulty has extended to other types of wavelength-scale cavities, such as small-diameter microdisks [13, 14]. Typically, there have been two techniques to probe Q factors in wavelength-scale cavities. In the first, the microcavities are fabricated in an active emitter material (such as a quantum well or quantum dot epitaxy), the cavities are optically pumped, and the emitted resonance linewidth is studied subthreshold, near material transparency [13, 43, 12]. This technique is limited both by difficulties in accurately establishing the pump power at which transparency occurs and by the necessity that the cavity contain embedded emitters. In particular, the latter requirement limits the variety of material systems in which the cavity can be fabricated (silicon, for example, would not be an easy option) and is not suitable for passive resonators in devices such as filters. For such devices, a second technique, consisting of fabricating an on-chip in-plane waveguide to couple to the cavity, is often used [130, 49]. In this approach, the problem of coupling light into the cavity is shifted to that of coupling light into the on-chip waveguide, a technically less challenging problem that can be done through a number of end-fire based approaches. A limitation of this technique is that it lacks a certain amount of flexibility due to the necessity of fabricating an in-plane waveguide for each cavity on the chip. In addition, both this approach and the emission-based approach described above do not provide a means to probe the V_{eff} of the cavity. To address this, several researchers have begun to investigate photonic crystal microresonators using near field scanning optical microscopy (NSOM), taking advantage of the sub-wavelength resolution that can be achieved in such measurements to map the localization of the cavity modes [131, 132].

The technique we have described in this chapter employs an *external* waveguide to couple to the cavity, where the external waveguide is a tapered optical fiber. Tapered optical fibers have been successfully used in the past to excite the resonances of larger sized microcavities, such as silica microspheres [32, 20] and microtoroids [56], and more recently, to excite the modes of a silicon-based PC waveguide [38, 40]. In these implementations, phase matching between the mode of the taper and the traveling wave mode of the resonator or the propagating mode of the waveguide was critical in achieving highly efficient coupling [55, 39]; in the former case, phase matching occurred primarily due to the silica-silica interface (same material index) between the taper and the microsphere, while in the latter, the dispersion of the PC waveguide was engineered to compensate for the disparate material indices (n=3.4 for silicon and $n = 1.45$ for silica) and achieve a PC waveguide effective index that matched that of the taper.

To study wavelength-scale cavities, we no longer rely on achieving phase matching, but rather just use the taper as a convenient means to produce a micron-scale evanescent field for sourcing and out-coupling the micron-scale cavity field. The taper effectively serves to bridges the disparate length scales from conventional fiber and free-space optics to chip-based microoptics, and does so entirely off the chip, so that on-chip structures do not require any additional complexity. Although the coupling we observe might not be as efficient as phase matched coupling, the power transfer is more than adequate enough to probe many of the important properties of the cavity. By using an external waveguide as the coupling element, this method is inherently non-invasive, can be used to rapidly characterize multiple devices on a chip, and the ability to vary the position of the taper with respect to the cavity (not an option for microfabricated on-chip waveguides) allows for quantitative investigation of not only the Q factor but also V_{eff}. Furthermore, the resonant coupling from the external waveguide is polarization selective, providing additional information about the cavity modes that is not easily obtainable through techniques such as NSOM. Knowledge of a mode's spectral position, polarization, Q, and V_{eff} will in many cases be enough to unambiguously determine the identity of the mode in comparison to simulation or theoretical results. Thus, in some respects, the versatility of the fiber-based approach that we have described in this chapter makes the technique an optical analog to electrical probes used to study microelectronic devices.

Another important aspect of this technique is the speed with which measurements can be made. In particular, the critical alignment step required in this work is making sure that the taper is not angled with respect to the surface of the chip, to ensure that coupling only occurs between the taper and the cavity, and not some extraneous part of the chip. Once this is done, and once the taper is aligned along the desired axis of the cavity, all of the devices within an array can be rapidly tested, and the spectral positions of resonances in successive devices can be determined within tens of seconds or faster. As an illustration of this, a movie showing the testing of two adjacent PC cavities has been made and is freely available on the internet (http://copilot.caltech.edu/research/PC_cav.avi). This ability to easily probe an array of devices on a chip greatly speeds up the testing process and shortens the turnaround time between device fabrication and measurement. Furthermore the simplicity of the measurement technique is another attractive feature; a single fiber taper serves as both the excitation and collection probe, and the taper is physically robust enough (will not break) so that no active servo control of the taper position is required to prevent it from touching the sample surface (in contrast to the more delicate probes used in NSOM techniques [132]).

Finally, we note that the optical fiber taper probe can be used to examine the spectral and spatial properties of a number of wavelength-scale microcavities, and is not limited to just PC microcavities. The suitability of the fiber taper as a probe for a given microcavity will in large part be determined by the overlap between the cavity and taper fields; simply put, if that overlap is sufficiently large, an appreciable amount of power can be transferred from the taper to the cavity even without phase matching (in general, phase matching will not be achieved, because of the index mismatch between the silica fiber taper and the high refractive index semiconductors typically used in wavelength-scale cavities). For the A_2^0 PC microcavity mode studied in this work, the depth of coupling is typically limited to $\sim$ 10%-20%, and at maximum levels of coupling, the cavity Q is degraded due to the taper loading effects seen in fig. 4.6. However, due to the low-loss nature of the optical fiber tapers (insertion losses are routinely as low as 10%), this is still a significant amount of coupling into the cavity, and from the measurement standpoint, coupling levels of a few percent are easily adequate to discern cavity resonances in the taper's transmission, and to then probe the Q and V_{eff} of the cavity. For applications requiring highly efficient power transfer from the fiber into the cavity, other approaches using an intermediate photonic crystal waveguide coupler have been developed [57], and will be briefly described in the following section.

As an example of the application of this probing technique to other types of wavelength-scale microcavities, fiber tapers have recently been used to probe the spectral and spatial properties of whispering gallery modes in $d < 10$ μm diameter silicon microdisks [64] and AlGaAs microdisks with embedded quantum dots [69] (the latter of which will be described in detail in the second part of this thesis). Because the radiation losses in high-index-contrast microdisks are quite low ($Q_{\text{rad}} > 10^8$), measurements of Q in fabricated devices is a simple and elegant way to determine etch-induced and bulk material losses within a given materials system [65, 128], allowing one to optimize an etching process for the creation of low-loss structures. Because the fiber taper measurement is a passive measurement (light-emitting material is not required), this probing technique provides optical access to materials systems, such as silicon, which otherwise could only be accessed via end-fire coupling to microfabricated on-chip waveguides. We briefly review some of the results on Si microdisks in the following section.

4.8 Efficient optical fiber coupling to photonic crystal microcavities and microdisks

4.8.1 PC microcavities

To this point, we have demonstrated a PC microcavity that has a sufficiently high Q and small V_{eff} to enable strong coupling experiments in cQED, and we have shown that the Q is relatively robust to fabrication imperfections. To do these measurements, we have used fiber tapers as a way to couple light into and out of these devices. The above sections have detailed how the fiber taper can serve as a very versatile probe for studying the spectral and spatial properties of PC cavity modes.

One thing that was not shown in the measurements above is that the fiber taper is an efficient way to get light into and out of the PC cavities, and indeed, to this point, it has not been. In particular, depths of coupling between the taper and cavity have been limited to values around 10%, and at these highest levels of coupling, the Qs are significantly degraded (by about a factor of 2). It should be emphasized that whenever light is coupled out of a cavity, its Q is going to be degraded relative to its cold-cavity value. The important point is that the loss that is induced by coupling should be effectively funneled into some collection channel (this loss can euphemistically be called ’good’ loss). For the direct fiber taper probing measurements, this clearly is not the case; the Q is degraded by almost a factor of 2, indicating that significant loss has been induced by the interaction with the taper, but only a small fraction of this loss has been collected, as evidenced by the small depths of coupling. The additional (uncollected) loss, which we call ’bad’ loss, might be due to scattering or coupling into undesirable taper modes. For cavity QED applications, the goal is to obtain a requisite signal level without degrading the Q so far that the cavity is no longer in the strong coupling regime. The ability to do this is somewhat compromised by the amount of ’bad’ loss present in the direct probing method; nevertheless, its simplicity makes it a candidate for use in future experiments.

The ability to efficiently source and extract light from the cavity is of particular importance for the low light intensities within the cavity in cavity QED experiments, where maximizing the amount of out-coupled signal from the interaction is necessary. In a standard Fabry-Perot cavity, the solution is perhaps obvious; one of the etalon mirrors is made to have slightly lower reflectivity. This causes a degradation of the cavity Q, but this additional loss is ‘good’ in the sense that it can be collected to comprise the measurement signal. Similarly, in a micropillar cavity, the top DBR mirror can be tailored to allow light to leak vertically into the air, where it can be efficiently collected into

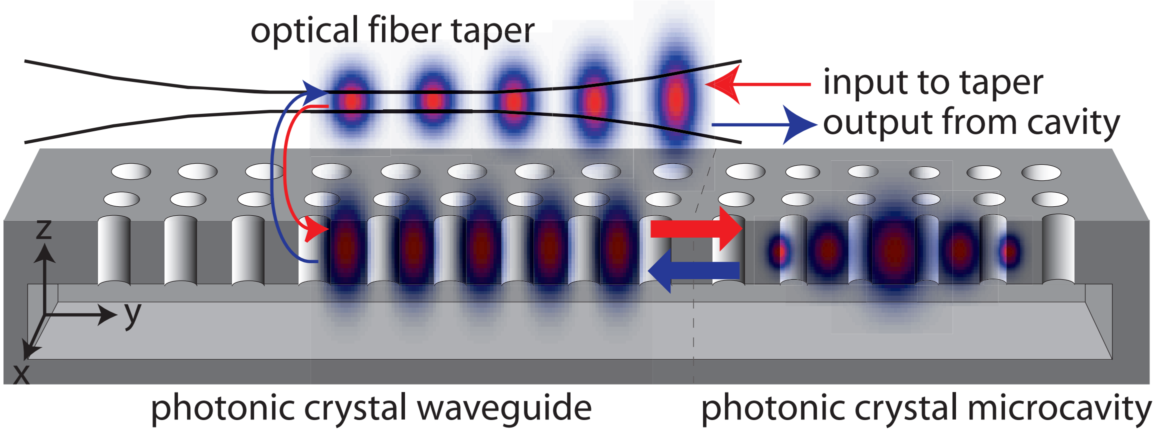

Figure 4.12: Fiber-coupled PC microcavity using an intermediate PC waveguide. (i) the taper adiabatically converts light injected into its input to a micron-scale field,(ii) light is contradirectionally coupled to a phase matched PCWG with high (> 95%) efficiency, (iii) light tunnels from the end of the PCWG into a mode-matched PC cavity, (iv) coupling from the cavity back to the fiber follows the reverse process, so that the output from the cavity is detected in the reflected signal at the fiber input. Refer to the paper of Barclay et al., for details [57].

an optical fiber [133]. However, in PC microcavities, the solution is not necessarily straightforward; their wavelength-scale modal patterns are typically not suited for direct mode matching to the much larger standard free-space and fiber optics. One solution is to integrate the cavity with an on-chip photonic crystal waveguide (PCWG), and then use various end-fire-based approaches to couple into and out of the PCWG. Despite significant improvement in techniques for such end-fire coupling, losses of $>$ 1 dB per coupling junction can still be expected in such systems [134].

To minimize the amount of ’bad’ loss when coupling to the cavities while still taking advantage of the desirable properties of fiber tapers, my colleague Paul Barclay developed a technique that makes use of an intermediate photonic crystal waveguide (PCWG) [57]. In this approach (fig. 4.12(a)), light is first efficiently ($>$ 95%) transferred to the PC chip by phase matched evanescent coupling between an optical fiber taper and a PCWG [39]. This coupling is so efficient because the PCWG has been designed to phase match to the mode of the optical fiber taper (not the case in direct coupling between the fiber and cavity), and has a significant enough spatial overlap with it for near-complete power transfer over tens of microns. The PCWG is terminated by the PC cavity; the two devices have been designed to be mode matched so that coupling between them is also very efficient. Thus, light propagates through the PCWG, and when it reaches the PC cavity termination, some amount of the light that is resonant with the cavity mode tunnels into it (the amount of tunneling can be adjusted by tailoring the PCWG-PC cavity junction). This light can then interact with material in the cavity (an atom or quantum dot, for example), and then tunnel back into the PCWG, where it will be transferred back into the reflected signal of the optical fiber for measurement. Experimental measurements of fabricated Si devices have yielded an unoptimized fiber-to-cavity coupling efficiency of 44% for a cavity with a loaded (unloaded) Q of 38,000 (47,000). Importantly, the limitations on the demonstrated coupling efficiency were not fundamental, but due to technical reasons, such as non-ideal taper-PCWG coupling and an imperfectly tailored PCWG-PC cavity transition region.

4.8.2 Microdisk cavities

Complementing the work described in the previous sections of this chapter, my colleague Matt Borselli has investigated silicon microdisk cavities, of the geometry shown in fig. 4.13. Microdisk cavities support whispering gallery modes (WGMs) in which light circulates around the periphery of the structure and is confined by total internal reflection at both the curved interface and the top and bottom surfaces. In comparison to microsphere cavities [19, 20, 135], microdisks are an optically thin dielectric slab in one dimension, which serves the dual purpose of dramatically reducing the number of modes within the structure, as well as the volume of those modes.

These microdisk cavities were of particular interest because they could support modes with very high radiation-limited quality factors ($Q_{rad} \sim 10^8$) for all but the smallest diameter structures (this was verified by finite-element-method simulations [136, 128, 137]). This is a result of the large refractive index contrast between the Si ($n \sim$3.4) layer and the surrounding air (n=1). This large index contrast also suggests that modes with a much tighter spatial confinement (i.e., a smaller V_{eff}) than what is available in glass microcavities [19, 20, 56] can be supported. In addition to their potential Q and V_{eff} values, these cavities can be fabricated using the exact same fabrication processes developed above (section 4.2), and can be probed using optical fiber tapers.

Reference [64] describes the first set of results obtained from these devices. Cold-cavity Qs as high as $\sim 5{\times}10^5$ for $V_{\text{eff}} \sim 6(\lambda/n)^3$ were demonstrated, as were loaded Qs of $\sim 1.5{\times}10^5$ for a taper-cavity coupling depth of $\sim$ 50%. Since these initial results, Matt and another colleague, Tom Johnson, have gone on to show that they could reach Qs as high as $5.0{\times}10^6$, albeit in larger volume devices [65], and have achieved critical coupling and overcoupling to these devices [128]. These high Qs have been achieved through additional improvements to the fabrication procedure described earlier, including the use of a resist reflow process to ensure very circular disk geometries [65], and a sequence of cleaning steps at the end of the disk fabrication aimed at the removal of

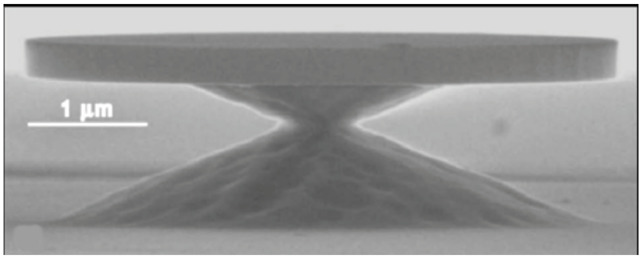

Figure 4.13: Scanning electron microscope image of a silicon microdisk cavity. Refer to the paper of Borselli et al., for further details [64].

highly absorbing surface layers from the devices [128].

From the perspective of the cavity QED experiments that have been a focus of this thesis, these Si microdisk cavities are extremely appealing, particularly in conjunction with integrated self-assembled quantum dots (QDs), where the field of the microdisk can optimally spatially overlap with the QD. Although PC cavities can ultimately result in similar or even better performance in terms of metrics such as Q/V_{eff} [52, 51, 28, 30], and can be effectively coupled to through the use of photonic crystal waveguides integrated with optical fiber tapers [57], these microdisk cavities are quite competitive on both the Q/V_{eff} and coupling fronts. More importantly, the simplicity of direct fiber coupling (rather than use of an intermediate element as is necessary for the PC cavities) and the relative ease of fabrication of these devices make them promising candidates for initial experiments. This is described in further detail in the upcoming chapters.